Check for updates

Optoacoustic imaging in endocrinology and metabolism

Angelos Karlas[1,2,3,4], *Miguel A. Pleitez*[1,2], *Juan Aguirre*[1,2] *and Vasilis Ntziachristos*[1,2] ✉

Abstract | Imaging is an essential tool in research, diagnostics and the management of endocrine disorders. Ultrasonography, nuclear medicine techniques, MRI, CT and optical methods are already used for applications in endocrinology. Optoacoustic imaging, also termed photoacoustic imaging, is emerging as a method for visualizing endocrine physiology and disease at different scales of detail: microscopic, mesoscopic and macroscopic. Optoacoustic contrast arises from endogenous light absorbers, such as oxygenated and deoxygenated haemoglobin, lipids and water, or exogenous contrast agents, and reveals tissue vasculature, perfusion, oxygenation, metabolic activity and inflammation. The development of high-performance optoacoustic scanners for use in humans has given rise to a variety of clinical investigations, which complement the use of the technology in preclinical research. Here, we review key progress with optoacoustic imaging technology as it relates to applications in endocrinology; for example, to visualize thyroid morphology and function, and the microvasculature in diabetes mellitus or adipose tissue metabolism, with particular focus on multispectral optoacoustic tomography and raster-scan optoacoustic mesoscopy. We explain the merits of optoacoustic microscopy and focus on mid-infrared optoacoustic microscopy, which enables label-free imaging of metabolites in cells and tissues. We showcase current optoacoustic applications within endocrinology and discuss the potential of these technologies to advance research and clinical practice.

Imaging has a critical role in the morphological and functional visualization of organs and tissues in vivo and is widely used to assess various endocrine disorders in the pituitary, thyroid, adrenal and reproductive glands, the pancreas, bone and different forms of endocrine tumour[1]. Many of the imaging modalities that are in use can exploit intrinsic tissue contrast; however, techniques also commonly utilize contrast agents to reveal morphological, physiological and biochemical features[2]. Generally, ultrasonography, X-ray CT and MRI are used for anatomical and physiological imaging of glands or lesions using either intrinsic contrast or contrast agents. In addition, scintigraphy, positron emission tomography (PET) and single-photon emission computed tomography (SPECT) imaging extend visualization at the functional and molecular level of the disease, measuring biochemical and metabolic parameters using externally administered radionuclide-based agents (TABLE 1). Despite this wealth of imaging options, a need still exists for portable, low-cost and easily disseminated methods that can be safely applied to large populations to assess endocrine and metabolic diseases, which are highly prevalent[3].

Optical imaging in the visible (380–750 nm) or near-infrared (NIR; 750–2,500 nm) wavelengths has been considered an alternative modality to traditional imaging methods for endocrinology applications. For example, fluorescence imaging using the fluorescent dye indocyanine green, or parathyroid autofluorescence have been used in endocrine surgery. Specifically, adrenalectomy or thyroidectomy operations have been performed under fluorescence guidance that in the latter scenario improves the detection of the parathyroid glands, which are difficult to identify and are often unnecessarily excised along with the thyroid[4]. In particular, label-free autofluorescence imaging shows good potential for detecting parathyroid tissue during surgery[5]. However, this method has limited penetration depth (~3 mm) and does not provide information about parathyroid tissue perfusion and oxygenation, which are crucial factors for the preservation of the parathyroid glands during surgery[5].

Hyperspectral imaging (HSI) is a method that collects images of tissue at multiple wavelengths. This technique has also been used intraoperatively to discriminate between thyroid and parathyroid tissues based on spectral changes, which are exhibited owing to differences in the concentration of haemoglobin and oxygenation, as well as water and lipid content[6]. Like conventional

[1]*Chair of Biological Imaging, Center for Translational Cancer Research (TranslaTUM), Technical University of Munich, Munich, Germany.*

[2]*Institute of Biological and Medical Imaging, Helmholtz Zentrum München, Neuherberg, Germany.*

[3]*Department of Vascular and Endovascular Surgery, Klinikum rechts der Isar, Technical University of Munich, Munich, Germany.*

[4]*Munich Partner Site, German Center for Cardiovascular Research (DZHK), Munich, Germany.*

✉*e-mail: v.ntziachristos@tum.de*

https://doi.org/10.1038/s41574-021-00482-5

Key points

- Optoacoustic technology includes a range of non-invasive, label-free and portable imaging modalities, which provide molecular visualizations at the macroscopic, mesoscopic and microscopic scale.
- Multi-spectral optoacoustic tomography produces real-time tomographic views of tissue with a resolution of 200–300 μm (macroscopy) at depths of 2–4 cm.
- Raster-scan optoacoustic mesoscopy provides volumetric images of tissue microvasculature and perfusion with a resolution of <10 μm (mesoscopy) at depths of 1–2 mm.
- Mid-infrared optoacoustic microscopy provides label-free visualizations of the spatiotemporal dynamics of biomolecules in cellular metabolism.
- Optoacoustic imaging offers a complete framework for investigating anatomic, functional and molecular aspects of common endocrine disorders.

photography, HSI achieves good spatial resolution (25 μm per pixel[7]) but its penetration depth is shallower than that of fluorescence imaging. Consequently, HSI can only be used to assess the very superficial layers of tissue, which limits its overall accuracy and diagnostic potential in tissue applications[7,8].

Optical visualization deeper in tissue has been achieved by diffuse optical tomography (DOT), which is a technique that records diffusive light (typically in the NIR range) that has propagated through tissue to a depth of several millimetres to centimetres. Being a tomographic technique, DOT uses mathematical inversion to compute maps of photon absorption and photon scattering in tissue, which are representative images of haemoglobin concentration and cellular density, respectively. The use of DOT for non-invasive endocrine imaging of the thyroid gland has been explored in computational experiments[9]. However, the strong photon scattering by tissue degrades spatial resolution as a function of depth (especially for depths more than 5 mm) and increases uncertainty about the recorded information, especially in terms of quantifying the absorption and scattering contrast. Owing to these limitations, DOT and related optical techniques have yet to find wide acceptance in clinical endocrinology.

Optoacoustic imaging is an alternative optical imaging modality that combines the advantages of optical contrast with the ability to provide high-resolution images deep inside tissue. However, while other optical techniques are sensitive to both optical absorption and scattering, contrast in optoacoustic imaging is primarily due to optical absorption only. In this modality, optical contrast is sensed by detecting ultrasound waves, which are excited within tissue, owing to the absorption of light of varying intensity by molecules that absorb the light energy (described in more detail later). Without the use of labels, optoacoustic imaging can resolve oxygenated haemoglobin and deoxygenated haemoglobin, melanin, lipids, collagen and water, on the basis of their absorption spectra, by recording optoacoustic images at multiple wavelengths and using spectral unmixing techniques. The technique has been considered since the late 1970s in imaging applications[10,11]. Furthermore, considerable progress was achieved in the following decades that enabled the imaging of tissues in vivo in animal models and in humans, resolving contrast from tissue vascularization and oxygenation[12–16]. Nevertheless, it is only in the past 5 years that the technology has sufficiently matured to enable high-performance biomedical imaging in humans outside dedicated laboratory settings[17–20].

A hand-held implementation of optoacoustics, termed multi-spectral optoacoustic tomography (MSOT), has been now uniquely used, in mice and humans, to assess a number of different conditions associated with endocrinology including oxidative metabolism[21,22], muscle oxygenation and hypoxia[23–25], cardiovascular imaging[26–29], muscular dystrophy[18], inflammation[17], and vascularization and total blood volume[27,30,31]. Importantly, visualization of these conditions is done without the use of contrast agents (label-free), often capitalizing on the use of two or more wavelengths to generate contrast based on the spectrum of intrinsic tissue light-absorbing molecules (discussed in detail later). Techniques such as raster-scan optoacoustic mesoscopy (RSOM) achieve superior image resolution but at a more superficial tissue depth[32]. By contrast, a 2019 study showed that optoacoustic microscopy extending to the mid-infrared spectral range (2,500–12,000 nm) could achieve unique visualization of proteins, carbohydrates and lipids in label-free mode[33]. More generally, optoacoustic imaging techniques, also referred to as 'photoacoustic' (for example, spectral photoacoustic tomography (sPAT) and photoacoustic microscopy (PAT))[34–36], have been also used in humans for imaging breast cancer[20,37] and arthritis[38], and for enabling measurements in animal models[35,39,40].

In this Review, we explore the current status and clinical potential of stand-alone MSOT, RSOM and hybrid optoacoustic and ultrasound systems. We explain the principle of operation of optoacoustic imaging and compare it with earlier investigations using optical imaging techniques. We elucidate the biomedical and clinically relevant information that is measured by the technique and focus in particular on label-free interrogations, that is, the types of imaging and contrast that can be achieved without the use of contrast agents. Finally, we describe current applications in endocrinology and discuss the clinical potential of the technology as a portable and safe method that offers high dissemination potential.

Principles of operation and contrast

Optoacoustic imaging is an optical imaging technique that illuminates tissue with transient light energy, commonly photon pulses in the nanosecond range[35]. Absorption of the excitation light by different molecules in tissue leads to the generation of fast thermoelastic expansions of the tissue at the site of absorption[41], giving rise to propagating ultrasound waves that can be detected with ultrasound detectors. The ultrasound waves are recorded in multiple positions on the tissue surface. For each detector position and photon pulse, a time-dependent ultrasound signal is recorded, with later times corresponding to optical contrast deeper in tissue and earlier signal times corresponding to shallower tissue. Subsequently, images of absorption are formed by mathematically combining all time signals recorded in all positions using image reconstruction techniques

Multi-spectral optoacoustic tomography
(MSOT). Macroscopic imaging technology that generates real-time images of tissues in clinical and preclinical applications.

Raster-scan optoacoustic mesoscopy
(RSOM). Mesoscopic imaging technology that produces volumetric images of tissues and is mainly used for skin and microvascular applications.

Chromophores
The parts of a molecule that absorb light at a particular frequency to give a molecule a specific colour.

(tomography)[12,32,42]. Optoacoustic imaging is fundamentally a three-dimensional imaging method, as ultrasound detectors can be placed around or scanned across tissue surfaces, thereby enabling imaging along two dimensions, while the depth (or the distance to detector, the third dimension) is retrieved from the time-dependent information contained in propagating ultrasound waves.

The detection of optical absorption using ultrasound detectors rather than optical cameras allows imaging with both high acoustic resolution and high optical contrast, as image formation is governed by the diffraction of generated ultrasound waves and not by the diffusion of light, as for example in DOT[43]. As an ultrasound detector is used for recording ultrasound signals, many optoacoustic implementations also use electronics that utilize the same ultrasound element for the generation of ultrasound waves, therefore also detecting ultrasound images in parallel to the optoacoustic images[28]. As light propagates in tissue much faster than sound, it is possible to send a light pulse and a sound pulse with a small time delay (in the microsecond range) between them and almost simultaneously record both ultrasound and optoacoustic waves for hybrid imaging.

Spectrum: the fourth dimension. Although images can be formed at a single wavelength, the illumination of tissue at several wavelengths (such as in MSOT) enables the detection of multiple images that provide a fourth dimension, that of the spectrum[12]. For example, a typical illumination pattern can scan a spectral range of 700–1,000 nm using 20 different wavelengths with a scan step of 15 nm. In this case, scans of each wavelength produce a stack of 20 images, that is, a 'multispectral stack'. The multispectral stack can be spectrally unmixed to quantify the concentration of different chromophores in each pixel of the reconstructed images. This spectral unmixing step uses the recorded MSOT data, as well as a library of known absorption spectra for specific chromophores that are relevant to each application, to produce a set of images that quantitatively map the distribution of the chromophores within the captured field of view (FIG. 1). Of note, a particular challenge in three-dimensional MSOT spectral unmixing (that is, across different tissue dimensions) is that the interaction between the illumination light and tissue depends non-linearly on depth and wavelength. This dependence produces a unique computational problem, which can compromise the quantification, the sensitivity and the specificity of spectral unmixing if not addressed. To overcome this issue, advanced non-linear spectral unmixing techniques have been proposed that provide improved accuracy for the identification of different chromophores in tissue as a function of depth[23,44].

Optoacoustic contrast and relation to endocrinology applications. Most optoacoustic clinical studies have focused on imaging intrinsic contrast in the NIR, that is, endogenous tissue chromophores (TABLE 2). The NIR is preferred as light can propagate for several centimetres in this spectral region. In particular, imaging oxygenated haemoglobin and deoxygenated haemoglobin in the 650–850 nm spectral window reveals information on tissue physiology that is associated with oxygenation and blood concentration[17,18,21,30]. The summation of oxygenated haemoglobin and deoxygenated haemoglobin relates to total blood volume, a parameter that is associated with inflammation[17,45], whereby the rate of total blood volume following tissue-activating stimulation (for example, cold exposure for brown adipose tissue (BAT)) is indicative of perfusion[21]. In addition, maps of tissue oxygen saturation (SO_2) can be computed as the ratio of oxygenated haemoglobin to total blood volume

Table 1 | **Imaging modalities in clinical endocrinology — uses, advantages and disadvantages**

Modality	Clinical use in endocrinology	Advantages	Disadvantages
Ultrasonography[110,111]	Imaging thyroid, parathyroid, adrenal and reproductive glands to assess diabetes mellitus (that is, imaging pancreas, kidneys, blood vessels, heart and/or adipose tissue) and endocrine tumours	Non-ionizing, real-time, fast, portable, easy to use, convenient for patient, high resolution-to-depth ratio, provides functional information	Low contrast, no direct molecular information, mediocre penetration depth
Plain radiography[112–114]	Imaging bone (for example, skeletal age, osteoporosis, hyperparathyroidism)	Fast, convenient for patient and practitioner, portable, high resolution-to-depth ratio	Ionizing radiation, low contrast, no molecular contrast, not real-time, no functional information, limited applications
CT[111,115–119]	Imaging adrenal, pituitary, thyroid and parathyroid glands, assessing diabetes mellitus (that is, imaging blood vessels, heart and/or adipose tissue), neuroendocrine tumours, bones	Whole-body imaging, high penetration depth, high resolution-to-depth ratio	Ionizing radiation, no direct molecular information, not real-time, long scanning times, inconvenient for patient, non-portable, requires trained specialist, mediocre contrast, possibly toxic contrast agents
MRI[111,116,117,120–123]	Imaging adrenal, pituitary, thyroid, parathyroid, bone, assessing diabetes mellitus (that is, imaging pancreas, kidneys, blood vessels, brain, heart and/or adipose tissue), neuroendocrine tumours, reproductive glands	Non-ionizing, whole-body imaging, high resolution-to-depth ratio, high contrast, real-time, functional information, might provide molecular contrast	Long scanning times, not portable, requires trained specialist, inconvenient for patient, might require contrast agents, costly
Scintigraphy, PET, SPECT[111,124–132]	Imaging thyroid, parathyroid, pituitary, adrenal, assessing diabetes mellitus (that is, imaging pancreas, blood vessels, brain, heart and/or adipose tissue), endocrine tumours, reproductive glands	Whole-body imaging, high resolution-to-depth ratio, high contrast, functional information, molecular contrast	Ionizing radiation, not real-time, contrast agents, long scanning times, not portable, difficult to use, inconvenient for patient

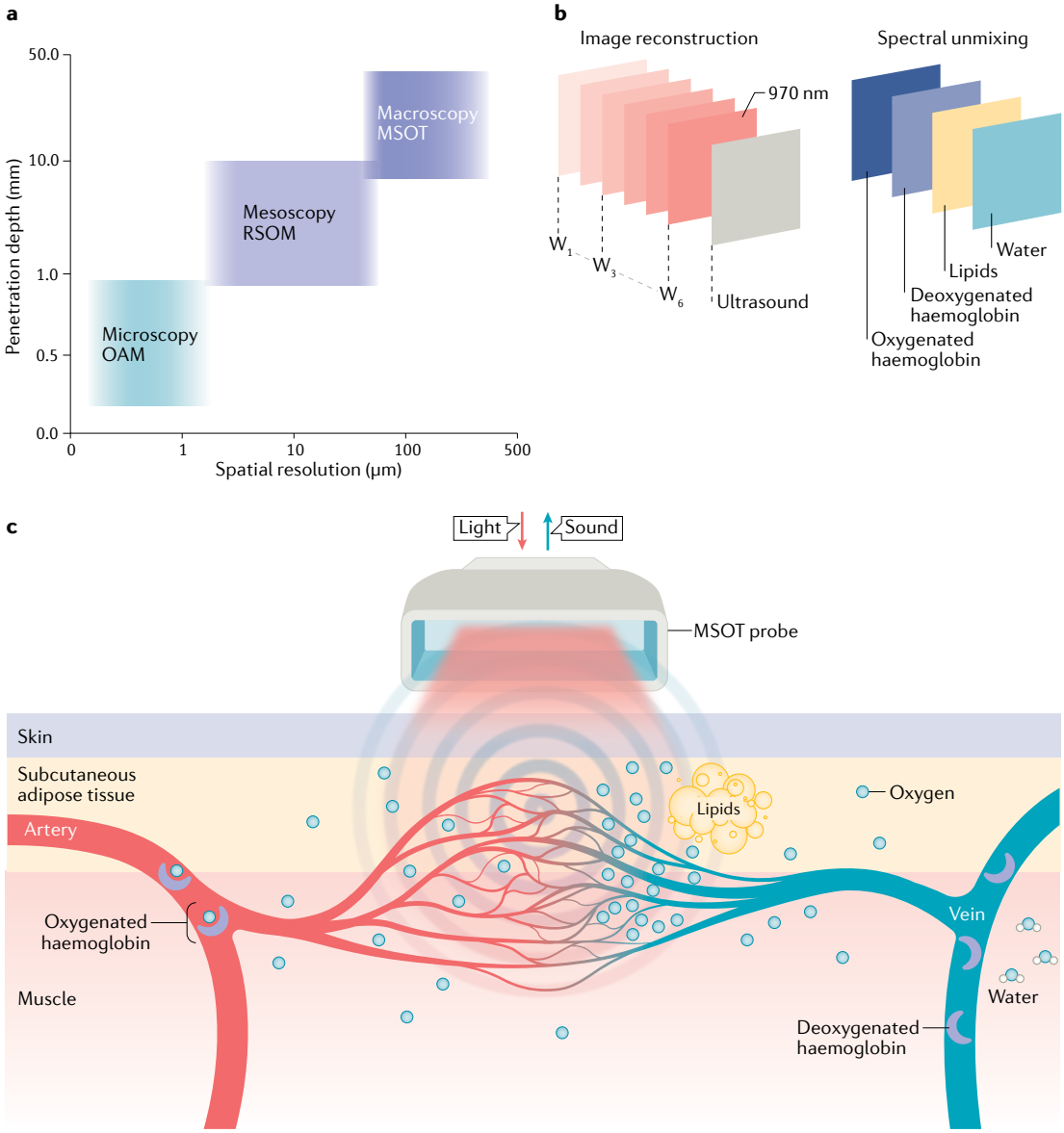

Fig. 1 | **Optoacoustic technology. a** | Classification of optoacoustic technologies according to penetration depth and resolution. **b** | For each optoacoustic frame, a corresponding ultrasound frame is recorded. Finally, recorded MSOT data (multispectral stacks of images taken at different wavelengths (W_x)) are spectrally unmixed into images showing the spatial distribution of chromophores, such as the oxygenated and deoxygenated haemoglobin, lipids and water. **c** | Light pulses (red arrow) of different near-infrared wavelengths illuminate tissue. The ultrasound waves (blue arrow) produced after the absorption of each light pulse are reconstructed into an optoacoustic frame. MSOT, multispectral optoacoustic tomography; OAM, optoacoustic microscopy; RSOM, raster-scan optoacoustic mesoscopy.

and the rate of SO_2 relates to oxygen utilization, that is, oxidative metabolism[17,23,24]. These parameters are relevant for various endocrine conditions, including thyroiditis, perfusion of thyroid nodules and parenchyma, hypoxia, vascularity and metabolic changes in tumours, as reviewed in the next section. Moreover, lipids can be sensed at 930 nm, where they exhibit an absorption peak[29,46] and these measurements can reveal parameters associated with white adipose tissue (WAT) and BAT, and the concentration of lipids in the bloodstream and specific tissue compartments. Such measurements relate to a number of pathologies associated with lipid disturbances, such as hyperthyroidism, obesity, polycystic ovary syndrome and thyroid or adrenal tumours. Finally, within the NIR region, water can be sensed at the 970 nm absorption peak[29]. Water measurements can be useful as reference measurements or in evaluating cystic structures in endocrine organs. Of note, studies have shown that it is possible to record collagen at the spectral peak of ~1,000 nm. This information could be useful in imaging patients with osteogenesis imperfecta, a genetic connective tissue disorder that affects several organs and tissues, such as the bones, skin, muscle and teeth[47,48].

Optoacoustic contrast can be enhanced with contrast agents, such as injected dyes, nanoparticles, and in animal models by the expression of a reporter gene[49,50].

Despite the large variety of agents examined in preclinical applications, only a few qualify today for clinical use. For example, indocyanine green is an organic dye that has been widely used for several clinical applications, including retinal angiography and hepatic clearance studies; notably, indocyanine green exhibits a high absorption cross-section in the NIR that can be detected with optoacoustics[51]. The use of gold nanoparticles has also been considered to improve optoacoustic image contrast owing to their ability to impart high contrast[52]. Finally, a new class of non-metal nanoparticle formulations is emerging that shows better photostability and even higher absorption cross-sections (and thus improved contrast) than gold particles[51,53]. However, the use of external contrast agents in humans requires rigorous safety evaluations and increases the cost and risk of an examination. Therefore, optoacoustic contrast agents are primarily used in animal studies[49,50].

Optoacoustic imaging implementations

Modern optoacoustic systems have been used for preclinical or clinical applications with a variety of configurations and technical specifications. In optoacoustic imaging, depth and resolution are inversely associated with the ultrasound detector frequency being used[12,54]. For example, by selective imaging at frequencies of a few megahertz (for example, central frequency of 4–6 MHz, bandwidth of 0.1–10 MHz), depths of 2–4 cm can be achieved with a resolution of 200–300 μm (that is, macroscopy). By contrast, imaging at frequencies in the tens of megahertz (for example, central frequency of 50 MHz, bandwidth of 10–100 MHz) enables imaging at depths of up to ~1 cm but with resolutions of a few tens of microns (that is, mesoscopy and microscopy) in a scalable fashion (FIG. 1). Of note, when ultrashort light pulses are used for excitation, all ultrasound frequencies in the tissue are excited. Finally, the use of detectors that capture frequencies at hundreds of megahertz (>100 MHz) approach resolutions that are typical of optical microscopy (<10 μm) at depths in the range of a few millimetres (1–2 mm). Alternatively, focused illumination can be used for optoacoustic microscopy, in direct analogy to optical microscopy. In this case, the tissue penetration is also typically sub-millimetre (<1 mm) but with resolutions that obey the laws of optical diffraction, with sub-micrometre lateral resolutions (<1 μm) being possible.

Macroscopy. The development of fast-tunable lasers with high energy per pulse[12,55] enabled real-time optoacoustic imaging at up to 100 frames per second, with each frame potentially being imaged at a different wavelength. Therefore, these lasers are appropriate for video rate multi-wavelength imaging that could reach five to ten MSOT frames per second. Detection is based on multi-element ultrasound arrays that detect frequencies in the 3–10 MHz range and corresponding analogue-to-digital converter arrays, which collect, digitize and store ultrasound signals in parallel and in real-time. For clinical applications (FIG. 2, FIG. 3), hand-held scanners (FIG. 1, FIG. 2a) are typically implemented in hybrid form with ultrasonography, utilizing the same common ultrasound detector array for the emission of ultrasound and detection of ultrasound and optoacoustic signals[21,29]. The same MSOT imaging principle also applies to the imaging of small animals (FIG. 4, FIG. 5). Animal imaging is performed using either hand-held systems or systems with dedicated small-animal imaging holders[21,56] (FIG. 4a). For the latter, the anaesthetized animal or a tissue sample of interest is typically placed in a cylindrical holder made of a transparent membrane. The membrane is surrounded by water to couple ultrasound to the transducer (another name for the device that records ultrasound). Although scanners for clinical applications cover angles of 100–180°, dedicated animal scanners can reach up to 270° for animals placed horizontally[57] or 360° for animals placed vertically into the imaging chamber[58]. Overall, higher angle coverage provides a more complete dataset and leads to improved imaging performance over smaller angle coverage.

Mesoscopy. Mesoscopy indicates higher resolution imaging (5–100 μm) but requires transducers that can collect higher frequencies and higher bandwidths than macroscopy (that is, they operate in the several tens of megahertz and higher, 10–100 MHz). Such high-frequency performance is not commonly achieved by detector arrays, which are generally limited to a few tens of megahertz (20–30 MHz)[59]. Therefore, high-performance mesoscopy is typically achieved with broad-band single-element detectors, which can operate at much higher frequencies. Owing to the use of a single element, mesoscopic imaging requires that the detector is scanned over the tissue, the implementation of which is termed RSOM[45,60] (FIG. 2c). Mesoscopy systems operating with detector arrays in the ~20 MHz range have also been reported[61].

The introduction of ultra-wideband (UWB) frequency detection, which reaches more than 200 MHz bandwidth, merges mesoscopic and microscopic resolutions in a single detector setup[32,62,63]. UWB RSOM has been used to assess the microvasculature in various organs in animals and humans, including human skin,

Table 2 | **Optoacoustic contrast**

Term[a]	Name	Feature visualized
HbO_2	Oxygenated haemoglobin	Vasculature (arteries, arterioles) and oxygenated haemoglobin in tissue
Hb	Deoxygenated haemoglobin	Vasculature (veins, venules) and deoxygenated haemoglobin distribution in tissue
$Hb+HbO_2$	TBV	Vasculature (total), inflammation
Ratio of HbO_2 to TBV	SO_2	Tissue oxygenation and hypoxia, vascular oxygenation
Change in TBV over time	TBV rate	Tissue perfusion
Change in SO_2 over time	SO_2 rate	Oxidative metabolism
Lipids	Lipids	Adipose tissue, lipid concentration in vasculature and tissue
Water	Water	Distribution of water in tissue

SO_2, oxygen saturation; TBV, total blood volume. [a]Physiological parameters that can be measured by optoacoustics based on endogenous light absorbers, such as haemoglobin, lipids and water.

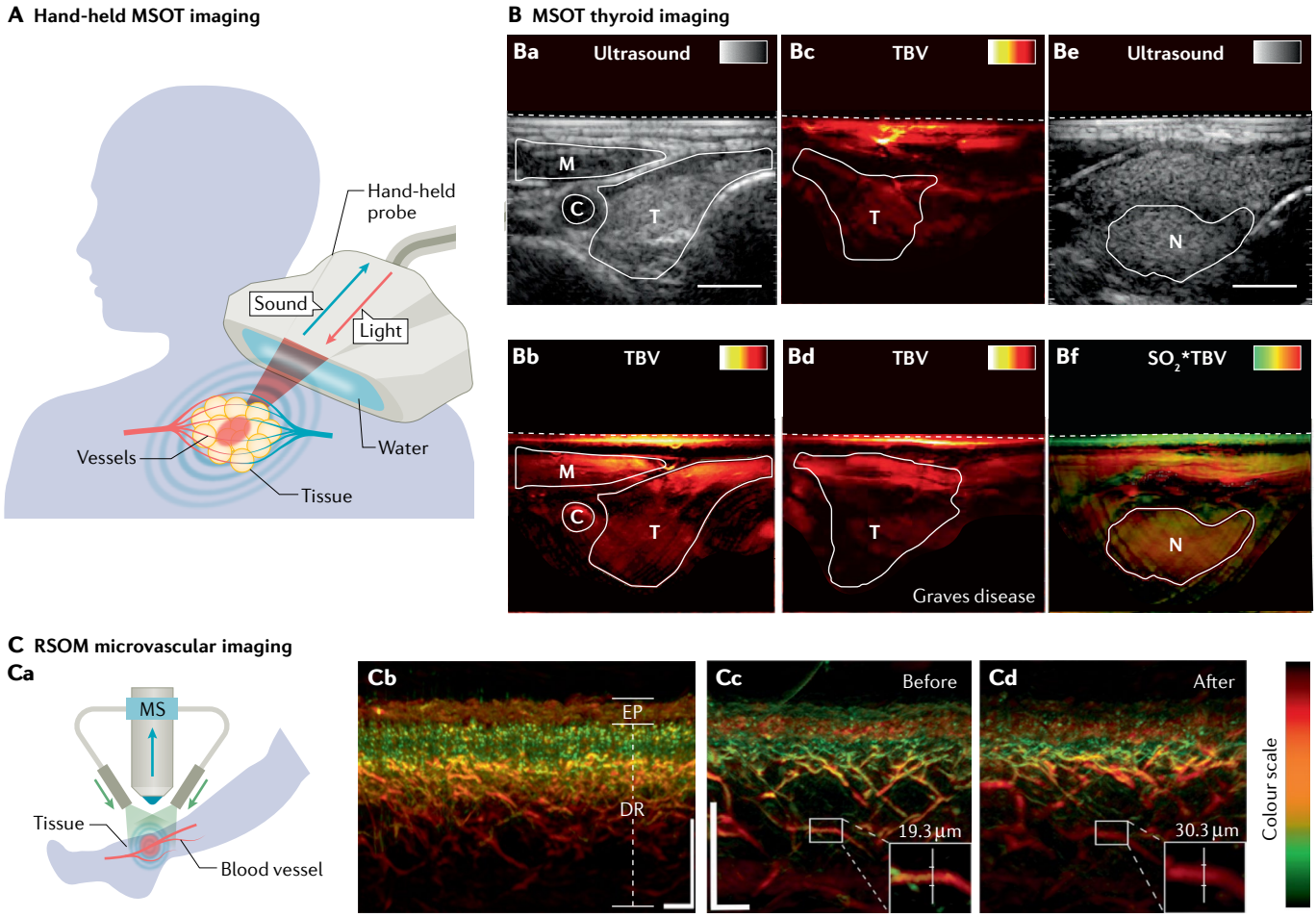

Fig. 2 | **Clinical optoacoustics in endocrinology: thyroid and microvascular imaging. A** | A hand-held optoacoustic unit. Light is shown as a red arrow and ultrasound as a blue arrow. The device comprises an ultrasound unit, an optoacoustic unit and a computer. **B** | Multispectral optoacoustic tomography (MSOT) imaging of the thyroid in healthy volunteers and patients. **Ba** | Ultrasound imaging of the neck in a healthy volunteer. **Bb** | Optoacoustic image of the total blood volume (TBV) for the ultrasound image of part **Ba**. **Bc** | Optoacoustic thyroid TBV image in a healthy volunteer. **Bd** | Optoacoustic thyroid TBV image in a patient with Graves disease. **Be** | Ultrasound image of a thyroid nodule. **Bf** | Optoacoustic oxygen saturation (SO_2) image weighted with the optoacoustic TBV signal (SO_2*TBV) corresponding to the ultrasound image of part **Be**. Scale bars represent 1 cm. White dashed line, skin. The colour scales range from minimum to maximum ultrasound or optoacoustic signal intensity. **C** | Skin microvascular imaging with raster-scan optoacoustic mesoscopy (RSOM). **Ca** | RSOM principle of operation. Motorized stages (MS) move the optical fibres, which deliver light (green arrows), and the ultrasound transducer, which records the produced ultrasound (blue arrow). **Cb** | RSOM image of skin vasculature. The colour scale represents the size of the imaged microvessels, with red representing large vessels, orange middle-sized and green small vessels. **Cc** | RSOM image of skin microvasculature before hyperthermia (inset: a small vessel with diameter 19.3 µm). **Cd** | RSOM image after hyperthermia (inset: same small vessel as in part **Cc** with diameter increased to 30.3 µm). Scale bars represent 0.5 mm. C, common carotid artery; DR, dermis; EP, epidermis; M, muscle; N, nodule; T, thyroid. Part **B**: this research was originally published in the *Journal of Nuclear Medicine*[77] Multispectral optoacoustic tomography of benign and malignant thyroid disorders–a pilot study. *J. Nucl. Med.* **60**, 1461–1466 (2019) © SNMMI. Part **Cb** is adapted from REF.[45], Springer Nature Limited. Part **Cc** and part **Cd** are adapted from REF.[67], CC BY 4.0 (http://creativecommons.org/licences/by/4.0/).

and enables imaging of capillaries close to the epidermis (<10 µm resolution) together with larger arterioles and venules of the deep vascular plexus[59,60]. Typically, the field of view of UWB RSOM spans tens of cubic millimetres, and images can be acquired in a few tens of seconds (15–45 s)[64]. Similar to MSOT, illumination at multiple wavelengths with RSOM allows visualization of oxygenated haemoglobin and deoxygenated haemoglobin (TABLE 2), which have been used to resolve microvasculature density, the distribution of oxygenated haemoglobin and deoxygenated haemoglobin, and SO_2 in tissue and microvessels[65]. Moreover, measurements of vessel size distribution and vessel density have been used to quantify skin inflammation[66]. Likewise, the imaging of lipids and water has been demonstrated with UWB RSOM and used to visualize tissue adipose tissue layers and the sebaceous glands[65]. Functional studies can also be performed by means of recording the endothelial-dependent hyperaemic response to a challenge, for example the application of a transient (for example, 3–5 min) cuff occlusion or heat[67–69]. Owing to the high resolution and contrast achieved by UWB RSOM, functional responses of the entire microvascular tree can be recorded in a label-free fashion[67].

Tyrosinase
An enzyme that facilitates the production of the pigment eumelanin and can be permanently expressed in engineered cells to provide strong optoacoustic contrast.

Mid-infrared optoacoustic microscopy
(MiROM). Label-free microscopic technology that provides endogenous biomolecular contrast images of cellular metabolites and their dynamics.

Microscopy. Like RSOM, optoacoustic microscopy also requires raster scanning, either of a high-frequency detector or a focused light beam[60]. Currently, optoacoustic microscopy lacks well-established labels for tagging cell function in comparison with optical microscopy, where fluorescence approaches are more refined. Although the use of tyrosinase[70] or other reporters and labels[71,72] has been researched, they have not shown the ubiquitous applicability of fluorescence proteins or agents in optical microscopy. For this reason, a driving force behind the development of optoacoustic operations are their integration with conventional optical setups, whereby optical performance is complemented by absorption contrast information that originates from optoacoustic detection. A promising demonstration of this premise is the use of optoacoustic microscopy at an extended spectral range in the infrared region. In particular, mid-infrared optoacoustic microscopy (MiROM) has been used in the spectral range of 2,500–12,000 nm[33,73] and has enabled the visualization of vibrational transitions of biomolecules, without the need for external labels[33]. MiROM can image proteins, carbohydrates and lipids within living cells, with a sensitivity better than that of Raman microscopy[74], which is an optical method that detects inherently weak inelastic scattering of photons.

Applications in endocrinology

Optoacoustic methods bring a unique label-free ability to record physiological tissue alterations caused by disease, which can be used for basic discovery, advancing diagnostics and monitoring disease progression and therapeutic efficacy. By being portable and using safe light energy, optoacoustic modalities are also appropriate for frequent and longitudinal measurements, and are compatible with the concurrent application of ultrasonography. The use of optoacoustic contrast agents in animal and cell research enables a large profile of biomarkers to be examined. These include features such as angiogenesis and vascular morphology, tissue oxygenation or hypoxia and metabolism[21], inflammation[17,30], lipids and water[29].

Thyroid disease. The thyroid gland is a highly vascularized organ that produces hormones, which affect organ function, metabolic rate and protein synthesis. Functional imaging of the thyroid offers diagnostics and theranostics (the combination of imaging and treatment delivery in a single system) in structural pathologies (that is, nodules and cancer) or functional pathologies (that is, hyperthyroidism or Graves disease, and Hashimoto thyroiditis or hypothyroidism)[75]. Current imaging techniques can either monitor the uptake of radioactive contrast agents using nuclear medicine techniques or assess blood flow in the thyroid by Doppler ultrasound.

MSOT could be used for enhanced functional characterization of the thyroid by imaging vascularization and oxygenation based on haemoglobin contrast, whereas imaging of lipid and water content can provide information on thyroid pathophysiology parameters. Importantly, initial studies in healthy volunteers[76] demonstrated the potential of MSOT to visualize vascular features of the thyroid gland. These studies stimulated

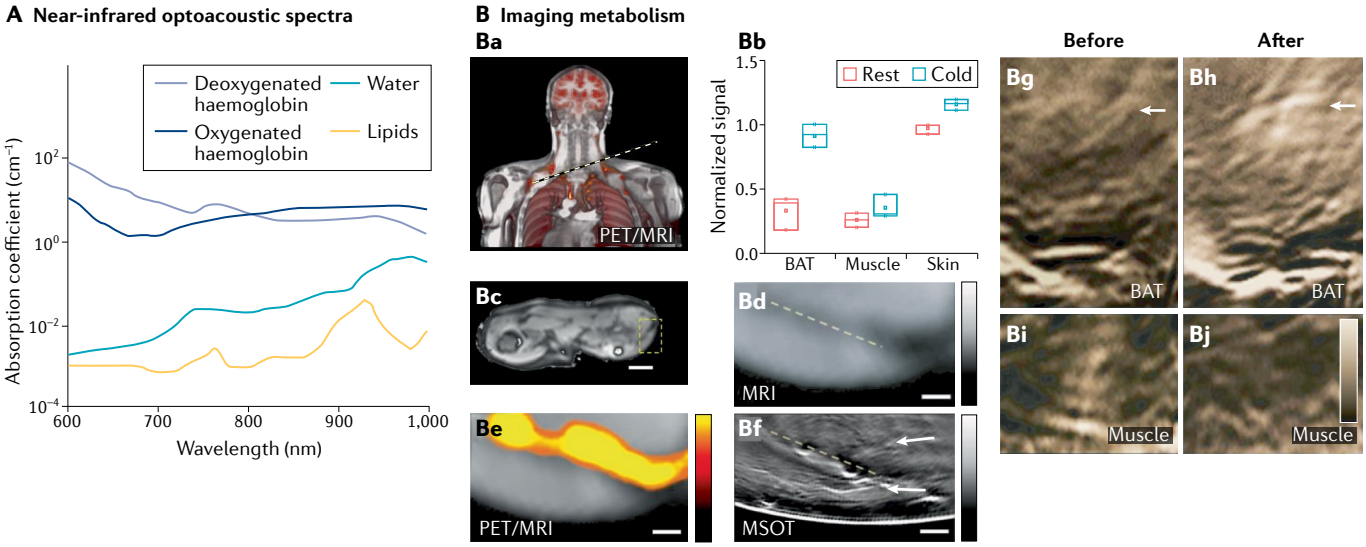

Fig. 3 | **Clinical optoacoustics in endocrinology: imaging metabolism.** **A** | Near-infrared absorption spectra of oxygenated haemoglobin, deoxygenated haemoglobin, lipids and water. **B** | Imaging metabolism with multispectral optoacoustic tomography (MSOT). **Ba** | PET–MRI of the brown adipose tissue (BAT) of a volunteer. **Bb** | Boxplots of the normalized optoacoustic signals within the BAT, muscle and skin before and after cold exposure (in three volunteers). **Bc** | MRI in the plane marked in part **Ba** with a dashed line. Scale bar represents 5 cm. **Bd** | MRI of the supraclavicular region marked with a yellow dashed box in part **Bc**. Scale bar represents 5 mm. The grey scale ranges from minimum to maximum MRI signal. **Be** | PET–MRI of the same region showing ^{18}F-fluorodeoxyglucose uptake within the BAT region (colour scale). Scale bar represents 5 mm. **Bf** | MSOT image of the same region. The grey scale ranges from minimum to maximum MSOT signal. Scale bar represents 1 mm. Top arrow, BAT; bottom arrow, muscle. **Bg** | BAT MSOT image before cold exposure corresponding to the region indicated by the top arrow in part **Bf**. **Bh** | Same region as in part **Bg** showing BAT after cold exposure. The arrow shows an increase in optoacoustic signal before and after BAT activation. **Bi** | MSOT image of muscle before cold exposure corresponding to the region indicated by the bottom arrow in part **Bf**. **Bj** | Same region as in part **Bi** showing muscle after cold exposure. The grey scale ranges from minimum to maximum MSOT signal. Part **B** adapted with permission from REF.[21], Elsevier.

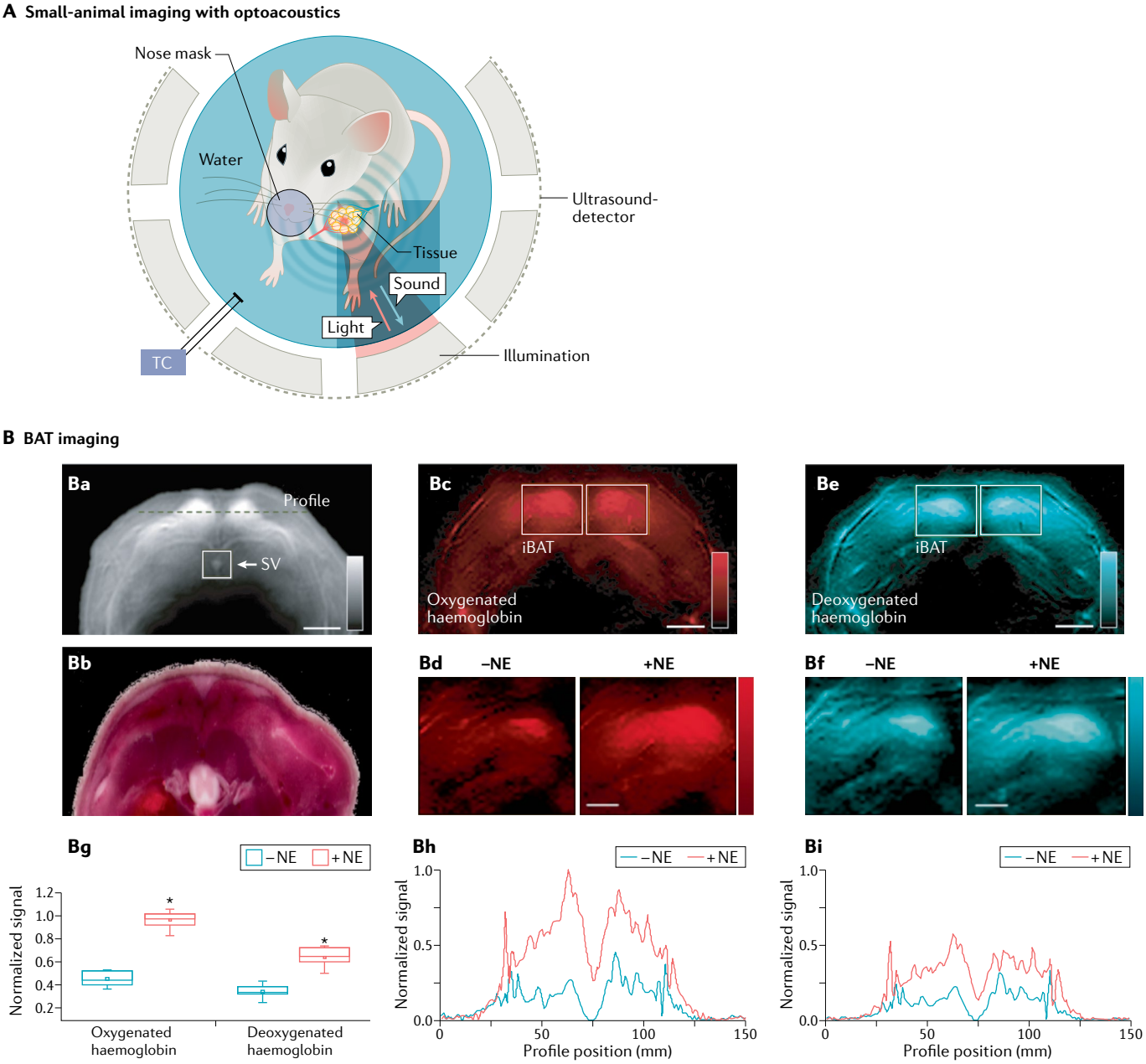

Fig. 4 | **Preclinical optoacoustics in endocrinology: imaging BAT.** **A** | Small-animal imaging with optoacoustics. Light is indicated by the red arrow and ultrasound by the blue arrow. The imaging station comprises an ultrasound unit, optoacoustic unit, anaesthesia unit, computer and a temperature controller (TC). **B** | Multispectral optoacoustic tomography (MSOT) of interscapular brown adipose tissue (iBAT) in a mouse. **Ba** | Anatomical optoacoustic image at 800 nm. **Bb** | Cryosection of same region. **Bc** | Optoacoustic image of oxygenated haemoglobin. **Bd** | Close-up view of iBAT-oxygenated haemoglobin before (–NE) and after (+NE) injection of noradrenaline. **Be** | Optoacoustic image of deoxygenated haemoglobin. **Bf** | Close-up view of iBAT-deoxygenated haemoglobin before (–NE) and after (+NE) noradrenaline injection. The scale bars for parts **Ba**, **Bc** and **Be** represent 4 mm; the scale bars for parts **Bd** and **Bf** represent 1 mm. **Bg** | Boxplot of normalized optoacoustic signal for iBAT-oxygenated haemoglobin and deoxygenated haemoglobin before (–NE) and after (+NE) noradrenaline injection. *$P < 0.01$. **Bh** | Normalized optoacoustic signal for oxygenated haemoglobin along the profile of part **Ba** before (–NE) and after (+NE) noradrenaline injection. **Bi** | Normalized optoacoustic signal for deoxygenated haemoglobin along the profile of part **Ba** before (–NE) and after (+NE) noradrenaline injection. The colour scale ranges from minimum to maximum optoacoustic signal. SV, Sulzer's vein. Part **B** is adapted with permission from REF.[21], Elsevier, and from REF.[133], Springer Nature Limited.

interest in optoacoustic imaging of thyroid anatomy (FIG. 2b) and function in diffuse thyroid diseases or nodular lesions, as well as the possibility of visualizing changes associated with malignancy without labels. In particular, MSOT revealed an increase in total blood volume and a reduction in lipid content within the thyroid parenchyma in patients with Graves disease ($n = 6$) compared with control individuals ($n = 8$)[77] (FIG. 2Bc, FIG. 2Bd). Furthermore, MSOT imaging showed the presence of hypoxia and reduced lipid content in patients with malignant thyroid nodules ($n = 3$) compared with people with benign thyroid nodules ($n = 13$)[77]

(FIG. 2Be, FIG. 2Bf). Furthermore, based on haemoglobin contrast, optoacoustic imaging could reveal small vessels in human thyroid cancers not visible by means of Doppler ultrasound, and provided functional parameters beyond the flow visualization that is provided by Doppler readouts[78]. These pilot studies showed the potential of MSOT to provide thyroid gland functional imaging without ionizing radiation or the injection of contrast agents. The short examination times (~5 min) and the portability of MSOT offer convenient use and could enable clinical dissemination.

Diabetes mellitus, obesity and metabolism. Diabetes mellitus is the most prevalent endocrine disease. Imaging in diabetes mellitus is important for visualizing the functional impairment of pancreatic β-cells and the effects of the disease on the cardiovascular, nervous, gastrointestinal, musculoskeletal and other systems[79,80]. Optoacoustic imaging could be used in patients to stage the severity of diabetes mellitus, by quantitative imaging of diabetic complications. For example, MSOT has been used to image the peripheral vasculature in healthy volunteers, as well as to assess endothelial macrovascular function in the radial artery[31], an early biomarker of atherosclerosis, which is accelerated in diabetes mellitus. Furthermore, based on haemoglobin contrast, MSOT showed promise in imaging the intestines in mice[81] and humans[17], as well as the haemodynamics and oxygenation of peripheral muscle in healthy volunteers[24] and patients with peripheral arterial disease[25], two organs that might be affected in patients with diabetes mellitus and manifest as diabetic enteropathy[82] or myopathy[83], respectively. Skin microvascular structure and reactivity can also be assessed by RSOM in great detail (FIG. 2c), and RSOM has been used in patients to characterize chronic inflammatory diseases, such as psoriasis[45]. These studies show that RSOM is a highly potent method for imaging skin micro-angiopathy, which is a quantitative indicator of diabetes mellitus[84–87]. Such microvascular impairments might appear before the development of clinically apparent symptoms associated with systemic manifestations of the disease[84]. Therefore, by using skin microvasculature as a biomarker of diabetes mellitus, RSOM could provide the means for portable characterization and precise staging of diabetic complications.

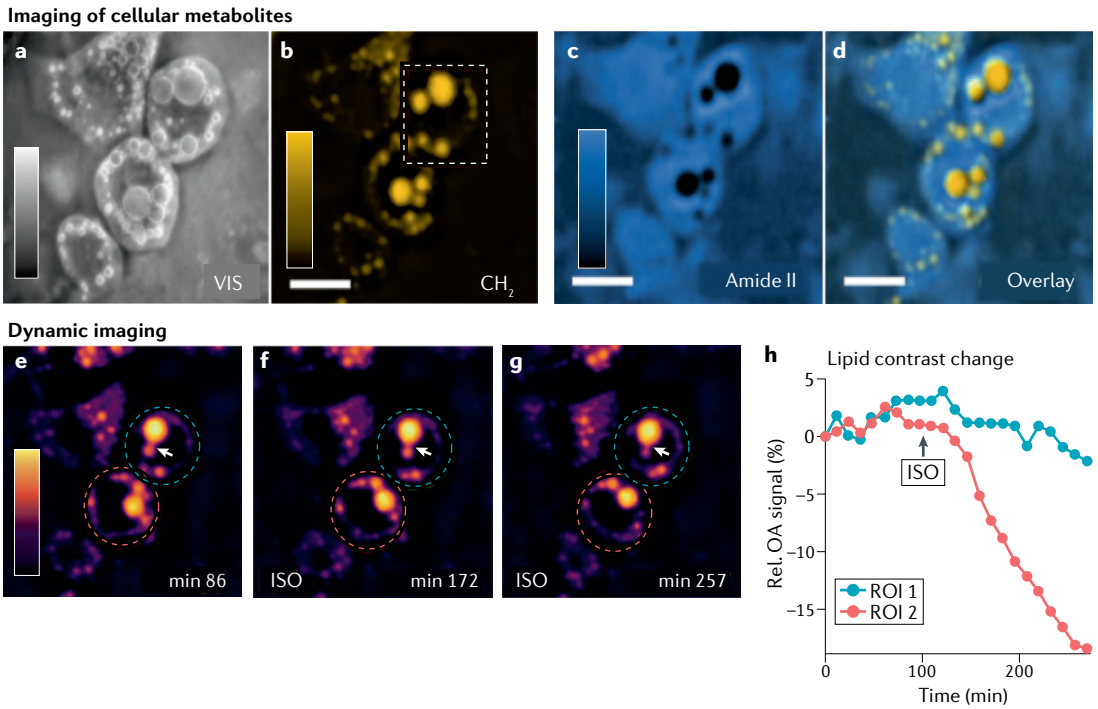

Fig. 5 | **Imaging of cellular metabolites using MiROM. a** | Bright-field image of 3T3-L1 cells that have been differentiated into adipocyte cells. **b** | Label-free mid-infrared optoacoustic microscopy (MiROM) image at 2,857 cm^{-1} wavenumber (CH_2 vibration: corresponding to the excitation of stretching vibrations of carbon–hydrogen bonds of the aliphatic tails of lipids) showing endogenous lipid contrast and corresponding to the image of a single adipocyte (dashed box). **c** | Label-free MiROM image at 1,550 cm^{-1} wavenumber (amide II) showing protein contrast over the same region. **d** | Overlay of lipid and protein maps over the same region. Colour scales range from minimum to maximum optoacoustic signal at the corresponding wavenumber. Scale bars represent 40 µm. **e**–**g** | Monitoring isoproterenol (ISO)-induced lipolysis in 3T3-L1 adipocytes using MiROM imaging at 2,857 cm^{-1} through time (part **e** corresponds to minute 86, part **f** to minute 172 and part **g** to minute 257). Blue (ROI 1) and red (ROI 2) dashed circles enclose two individual adipocytes. The white arrows follow the remodelling of a single lipid droplet after the addition of ISO. The colour scale ranges from minimum to maximum measured optoacoustic signal. **h** | Change in relative lipid contrast (Rel. OA signal) over time within the two individual adipocytes marked with dashed circles (blue (ROI 1) and red (ROI 2)) in parts **e**, **f** and **g**. The time point of ISO addition is indicated with the arrow (approximately minute 100). ROI, region of interest; VIS, visible light. Adapted from REF.[33], Springer Nature Limited.

In addition to haemoglobin contrast, MSOT can visualize lipids and adipose tissue (FIG. 3a) for assessing endocrine and metabolic functions. Recently, MSOT has been used to image lipid dynamics within human arteries, veins and soft tissues (subcutaneous adipose tissue and skeletal muscle) after the consumption of a high-fat meal[88]. The method has also been shown to resolve label-free WAT and BAT depots based on differences in the spectral profiles of the two tissue types[21]. Moreover, cold-induced BAT metabolic activation in volunteers was resolved (FIG. 3b) using optoacoustic imaging based on SO_2 rate contrast (TABLE 1). The ability to record metabolism using label-free optoacoustics has been further supported by mouse studies of BAT activation via noradrenaline injection (described later). Based on the same principle of vasometabolic coupling, whereby metabolic demand dictates blood flow and oxygen consumption, MSOT has been used in healthy volunteers to image muscle perfusion and oxygenation changes as a function of different challenges, such as exercise or blood supply occlusion[24,89]. In a 2019 study, RSOM was used to produce detailed images of intracutaneous lipids in humans along with several other endogenous chromophores (for example, haemoglobin, melanin and water)[65]. Dermal adipose tissue is also implicated in various conditions, including obesity and diabetes mellitus-related pathophysiology[90–92], and could be non-invasively investigated using optoacoustic techniques.

Surgical guidance in endocrine tumours. Optoacoustic imaging has been explored for surgical guidance, in particular for better localizing the tumour mass or to avoid damage to sub-surface vascular structures. This potential has been explored in various types of surgical procedure, including procedures for ovarian cancer[93] and pancreatic cancer[94], and surgery for endocrine tumours, that is, trans-sphenoidal surgical removal of pituitary tumours[95]. Furthermore, the use of optoacoustic guidance has been suggested for avoiding carotid artery trauma during surgical procedures of the pituitary, using a miniaturized optoacoustic warning device based on an optical fibre mounted on the surgical tool[96].

Research applications and animal studies. Optoacoustic imaging has been used as a research tool in many animal studies and can offer high-resolution whole-body imaging in mice. For example, protease activity was investigated in FTC133 thyroid tumours implanted in the hind legs of mice[97], using imaging agents sensitive to matrix metalloproteinases MMP2 and MMP9 resolved by small-animal MSOT. Optoacoustic imaging has also been used to characterize bone microstructure in an animal model of postmenopausal osteoporosis[98]. This study was conducted on excised femur bone specimens from female rats that had undergone ovariectomy, ovariectomy with intraperitoneal bone preservation therapy with zoledronic acid, or sham operation. The bone samples were examined by analysing the frequency spectra of the measured optoacoustic signals. Activation of BAT in mice was also possible based on recording the SO_2 rate (TABLE 2) after activation by noradrenaline[21], secretin[56] or icilin[99], which all induce BAT thermogenesis. In these studies, MSOT readouts showed a clear increase in both the oxygenated haemoglobin signal and the deoxygenated haemoglobin signal in activated BAT compared with BAT in the resting state (FIG. 4b). An increase in total blood volume within the interscapular BAT region after BAT activation was also recorded in these studies.

The development of MiROM[33] has led to its use, not only in small-animal research, but also in label-free imaging of metabolic parameters, such as lipids, carbohydrates and proteins in living cells (FIG. 5). For example, MiROM was used to visualize the spatiotemporal dynamics of lipid droplets during isoproterenol-induced lipolysis in brown adipocytes (derived from differentiated precursor BAT) and white adipocytes (differentiated 3T3-L1). Owing to its ability to visualize bond-specific molecular contrast, MiROM might enable the direct monitoring of hormones during metabolic processes. For instance, amino acid-based or protein-based hormones (such as insulin) could be detected using the amide I and amide II absorption bands, whereas steroids (for example, cortisol) could be detected by their absorption bands in the fingerprint region[100]. MiROM could be further combined with imaging in other spectral regions, such as the visible (380–750 nm) to observe tissue vascularization and oxygenation[101], or the NIR (780–2,500 nm) to monitor lipid metabolism[102]. Furthermore, MIROM can be easily combined with other microscopy techniques in multimodal hybrid setups[103] to reveal interesting crosstalk among several biological pathways[104–106].

Conclusions

Optoacoustic imaging offers four major strengths that drive its consideration in endocrinology studies. First, it solves the fundamental limitations of optical imaging, enabling for the first time high-resolution and quantitative imaging of chromophores deep in tissues in vivo. Second, it provides non-invasive, label-free imaging of contrasts that relate to tissue function and metabolism. Third, it can operate concurrently with ultrasonography, using the same ultrasound detector, enabling the simultaneous collection of complementary information. Finally, it offers portability and high safety so that it can be used for frequent and longitudinal studies.

The above-mentioned strengths of optoacoustic imaging come with limitations that could affect its usefulness for endocrinology. Despite reaching unprecedented depths at high resolution for a light-based imaging technique (for example, 2–4 cm for MSOT), optoacoustic imaging still offers poor penetration depths compared with other techniques (for example, PET, MRI or X-ray-based techniques; TABLE 1) owing to the attenuation of light energy with depth. Thus, imaging deeper organs (for example, pancreas or adrenal glands) or adipose tissue with optoacoustic techniques is a challenge. Furthermore, many current optoacoustic systems are hand-held, which necessitates a trade-off between practicality and accuracy. Hand-held probes are equipped with small ultrasound detector arrays in geometries that cover limited viewing angles (for example, 130–180°). The limited viewing angles introduce inaccuracies into the final representation of the true sizes of the anatomical structures and hinder precise interpretation of data. The

design of novel optoacoustic image reconstruction algorithms that compensate for the above-mentioned artefacts is expected to further improve the accuracy of recorded images. Moreover, optoacoustic imaging, especially clinical technologies (for example, MSOT and RSOM), are vulnerable to motion artefacts that degrade image quality. These artefacts might be patient-dependent (such as pulsation, breathing or voluntary patient motion) or operator-dependent (for example, irregular movements of the probe during scanning). Several algorithms have been developed to provide motion correction for microscopic, mesoscopic (for example, RSOM) and macroscopic (for example, MSOT) optoacoustic applications[107–109].

As different applications develop in endocrinology, we expect a disseminated use of the technology in studying metabolic and functional conditions associated with the progression of various diseases. Thus, optoacoustics could facilitate promising avenues of future research in the field of endocrinology, such as the investigation of adipose tissues in obesity and during obesity treatments, neuroendocrine tumours, diabetic microangiopathy and cellular lipid dynamics in cardiometabolic diseases, heading towards a more precise assessment of disease stage and the effects of possible interventions.

Published online 19 April 2021

1. Chrousos, G. P. Organization and integration of the endocrine system. *Sleep. Med. Clin.* **2**, 125–145 (2007).
2. Shaw, A. S. & Cheow, H. K. Imaging in endocrinology. *Medicine* **45**, 456–463 (2017).
3. Golden, S. H., Robinson, K. A., Saldanha, I., Anton, B. & Ladenson, P. W. Clinical review: prevalence and incidence of endocrine and metabolic disorders in the United States: a comprehensive review. *J. Clin. Endocrinol. Metab.* **94**, 1853–1878 (2009).
4. Kahramangil, B. & Berber, E. The use of near-infrared fluorescence imaging in endocrine surgical procedures. *J. Surg. Oncol.* **115**, 848–855 (2017).
5. Liu, J. et al. Near-infrared auto-fluorescence spectroscopy combining with Fisher's linear discriminant analysis improves intraoperative real-time identification of normal parathyroid in thyroidectomy. *BMC Surg.* **20**, 4 (2020).
6. Barberio, M. et al. Hyperspectral based discrimination of thyroid and parathyroid during surgery. *Curr. Dir. Biomed. Eng.* **4**, 399–402 (2018).
7. Halicek, M., Fabelo, H., Ortega, S., Callico, G. M. & Fei, B. In-vivo and ex-vivo tissue analysis through hyperspectral imaging techniques: revealing the invisible features of cancer. *Cancers* **11**, 756 (2019).
8. Kho, E. et al. Imaging depth variations in hyperspectral imaging: development of a method to detect tumor up to the required tumor-free margin width. *J. Biophotonics* **12**, e201900086 (2019).
9. Fujii, H., Yamada, Y., Kobayashi, K., Watanabe, M. & Hoshi, Y. Modeling of light propagation in the human neck for diagnoses of thyroid cancers by diffuse optical tomography. *Int. J. Numer. Method Biomed. Eng.* **33**, e2826 (2017).
10. Busse, G. & Rosencwaig, A. Subsurface imaging with photoacoustics. *Appl. Phys. Lett.* **36**, 815–816 (1980).
11. Rosencwaig, A. Potential clinical applications of photoacoustics. *Clin. Chem.* **28**, 1878–1881 (1982).
12. Taruttis, A. & Ntziachristos, V. Advances in real-time multispectral optoacoustic imaging and its applications. *Nat. Photonics* **9**, 219–227 (2015).
This paper provides a comprehensive overview of the MSOT technology and its applications.
13. Oraevsky, A., Jacques, S., Esenaliev, R. & Tittel, F. Laser-based optoacoustic imagin gin biological tissues. *Proc. SPIE 2134. Laser-Tissue Interaction V; and Ultraviolet Radiation Hazards* (eds. Jacques S. L., Sliney D. H. & Belkin M.) 122–128 (SPIE, 1994).
14. Oraevsky, A. A. et al. Laser optoacoustic imaging of the breast: detection of cancer angiogenesis. *Proc. SPIE 3597. Optical Tomography and Spectroscopy of Tissue III* (eds. Chance B., Alfano R. R. & Tromberg B. J.) 352–363 (SPIE, 1999).
15. Esenaliev, R. O. et al. Optoacoustic technique for noninvasive monitoring of blood oxygenation: a feasibility study. *Appl. Opt.* **41**, 4722–4731 (2002).
16. Esenaliev, R. O., Petrov, Y. Y., Hartrumpf, O., Deyo, D. J. & Prough, D. S. Continuous, noninvasive monitoring of total hemoglobin concentration by an optoacoustic technique. *Appl. Opt.* **43**, 3401–3407 (2004).
17. Knieling, F. et al. Multispectral optoacoustic tomography for assessment of Crohn's disease activity. *N. Engl. J. Med.* **376**, 1292–1294 (2017).
An original research paper on MSOT imaging of inflammatory bowel disease.
18. Regensburger, A. P. et al. Detection of collagens by multispectral optoacoustic tomography as an imaging biomarker for Duchenne muscular dystrophy. *Nat. Med.* **25**, 1905–1915 (2019).
An original research paper on MSOT imaging of collagen in Duchenne muscular dystrophy.
19. Stoffels, I. et al. Metastatic status of sentinel lymph nodes in melanoma determined noninvasively with multispectral optoacoustic imaging. *Sci. Transl Med.* **7**, 317ra199 (2015).
20. Menezes, G. L. G. et al. Downgrading of breast masses suspicious for cancer by using optoacoustic breast imaging. *Radiology* **288**, 355–365 (2018).
21. Reber, J. et al. Non-invasive measurement of brown fat metabolism based on optoacoustic imaging of hemoglobin gradients. *Cell Metab.* **27**, 689–701 (2018).
An original research paper on MSOT imaging of brown adipose tissue activation based on haemoglobin contrast.
22. Ntziachristos, V., Pleitez, M. A., Aime, S. & Brindle, K. M. Emerging technologies to image tissue metabolism. *Cell Metab.* **29**, 518–538 (2019).
This review provides a comprehensive overview of the novel technologies used in imaging metabolism.
23. Tzoumas, S. et al. Eigenspectra optoacoustic tomography achieves quantitative blood oxygenation imaging deep in tissues. *Nat. Commun.* **7**, 12121 (2016).
24. Karlas, A. et al. Multispectral optoacoustic tomography of muscle perfusion and oxygenation under arterial and venous occlusion–a human pilot study. *J. Biophotonics* **13**, e201960169 (2020).
25. Karlas, A. et al. Multispectral optoacoustic tomography of peripheral arterial disease based on muscle hemoglobin gradients–a pilot clinical study. *Ann. Transl Med.* **9**, 36 (2021).
26. Taruttis, A. et al. Optoacoustic imaging of human vasculature: feasibility by using a handheld probe. *Radiology* **281**, 256–263 (2016).
27. Masthoff, M. et al. Use of multispectral optoacoustic tomography to diagnose vascular malformations. *JAMA Dermatol.* **154**, 1457–1462 (2018).
28. Yang, H. et al. Soft ultrasound priors in optoacoustic reconstruction: improving clinical vascular imaging. *Photoacoustics* **19**, 100172 (2020).
29. Karlas, A. et al. Cardiovascular optoacoustics: from mice to men – a review. *Photoacoustics* **14**, 19–30 (2019).
30. Diot, G. et al. Multispectral optoacoustic tomography (MSOT) of human breast cancer. *Clin. Cancer Res.* **23**, 6912–6922 (2017).
An original research paper on MSOT imaging of human breast cancer.
31. Karlas, A. et al. Flow-mediated dilatation test using optoacoustic imaging: a proof-of-concept. *Biomed. Opt. Express* **8**, 3395–3403 (2017).
32. Omar, M., Aguirre, J. & Ntziachristos, V. Optoacoustic mesoscopy for biomedicine. *Nat. Biomed. Eng.* **3**, 354–370 (2019).
This paper provides a comprehensive overview of the RSOM technology and its biomedical applications.
33. Pleitez, M. A. et al. Label-free metabolic imaging by mid-infrared optoacoustic microscopy in living cells. *Nat. Biotechnol.* **38**, 293–296 (2020).
An original research paper on MiROM technology and its use in imaging of cellular metabolites.
34. Steinberg, I. et al. Photoacoustic clinical imaging. *Photoacoustics* **14**, 77–98 (2019).
35. Beard, P. Biomedical photoacoustic imaging. *Interface Focus.* **1**, 602–631 (2011).
36. Yao, J. & Wang, L. V. Photoacoustic microscopy. *Laser Photon. Rev.* **7**, 758–778 (2013).
37. Oraevsky, A. A. et al. Clinical optoacoustic imaging combined with ultrasound for coregistered functional and anatomical mapping of breast tumors. *Photoacoustics* **12**, 30–45 (2018).
38. Jo, J. et al. A functional study of human inflammatory arthritis using photoacoustic imaging. *Sci. Rep.* **7**, 15026 (2017).
39. Zhang, H. F., Maslov, K., Stoica, G. & Wang, L. V. Functional photoacoustic microscopy for high-resolution and noninvasive in vivo imaging. *Nat. Biotechnol.* **24**, 848–851 (2006).
40. Cox, B., Laufer, J. G., Arridge, S. R. & Beard, P. C. Quantitative spectroscopic photoacoustic imaging: a review. *J. Biomed. Opt.* **17**, 061202 (2012).
41. Wang, L. V. & Yao, J. A practical guide to photoacoustic tomography in the life sciences. *Nat. Methods* **13**, 627–638 (2016).
42. Lutzweiler, C. & Razansky, D. Optoacoustic imaging and tomography: reconstruction approaches and outstanding challenges in image performance and quantification. *Sensors* **13**, 7345–7384 (2013).
43. Ntziachristos, V. & Razansky, D. Molecular imaging by means of multispectral optoacoustic tomography (MSOT). *Chem. Rev.* **110**, 2783–2794 (2010).
44. Olefir, I., Tzoumas, S., Yang, H. & Ntziachristos, V. A Bayesian approach to eigenspectra optoacoustic tomography. *IEEE Trans. Med. Imaging* **37**, 2070–2079 (2018).
45. Aguirre, J. et al. Precision assessment of label-free psoriasis biomarkers with ultra-broadband optoacoustic mesoscopy. *Nat. Biomed. Eng.* **1**, 0068 (2017).
An original research paper on RSOM technology and its use in imaging of skin inflammation in psoriasis.
46. Shaw, A. & Mantsch, H. in *Encyclopedia of Analytical Chemistry* (eds. Meyers R. A. & Meyers R. A.) https://doi.org/10.1002/9780470027318.a0106.pub2 (Wiley, 2008).
47. Lindahl, K., Langdahl, B., Ljunggren, O. & Kindmark, A. Treatment of osteogenesis imperfecta in adults. *Eur. J. Endocrinol.* **171**, R79–R90 (2014).
48. Veilleux, L. N., Trejo, P. & Rauch, F. Muscle abnormalities in osteogenesis imperfecta. *J. Musculoskelet. Neuronal Interact.* **17**, 1–7 (2017).
49. Gujrati, V., Mishra, A. & Ntziachristos, V. Molecular imaging probes for multi-spectral optoacoustic tomography. *Chem. Commun.* **53**, 4653–4672 (2017).
50. Weber, J., Beard, P. C. & Bohndiek, S. E. Contrast agents for molecular photoacoustic imaging. *Nat. Methods* **13**, 639–650 (2016).
51. Beziere, N. et al. Dynamic imaging of PEGylated indocyanine green (ICG) liposomes within the tumor microenvironment using multi-spectral optoacoustic tomography (MSOT). *Biomaterials* **37**, 415–424 (2015).
52. Li, W. & Chen, X. Gold nanoparticles for photoacoustic imaging. *Nanomedicine* **10**, 299–320 (2015).
53. Gujrati, V. et al. Bioengineered bacterial vesicles as biological nano-heaters for optoacoustic imaging. *Nat. Commun.* **10**, 1114 (2019).
54. Ntziachristos, V. Going deeper than microscopy: the optical imaging frontier in biology. *Nat. Methods* **7**, 603–614 (2010).

55. Buehler, A., Kacprowicz, M., Taruttis, A. & Ntziachristos, V. Real-time handheld multispectral optoacoustic imaging. *Opt. Lett.* **38**, 1404–1406 (2013).
56. Li, Y. et al. Secretin-activated brown fat mediates prandial thermogenesis to induce satiation. *Cell* **175**, 1561–1574 (2018).
57. Park, S. J. et al. Visualizing Alzheimer's disease mouse brain with multispectral optoacoustic tomography using a fluorescent probe, CDnir7. *Sci. Rep.* **9**, 12052 (2019).
58. Ermilov, S. et al. 3D laser optoacoustic ultrasonic imaging system for research in mice (LOUIS-3DM). *Proc. SPIE 8943. Photons Plus Ultrasound: Imaging and Sensing* (eds. Oraevsky A. A. & Wang L. V.) 89430J (SPIE, 2014).
59. Schwarz, M., Omar, M., Buehler, A., Aguirre, J. & Ntziachristos, V. Implications of ultrasound frequency in optoacoustic mesoscopy of the skin. *IEEE Trans. Med. Imaging* **34**, 672–677 (2015).
60. Aguirre, J. et al. Broadband mesoscopic optoacoustic tomography reveals skin layers. *Opt. Lett.* **39**, 6297–6300 (2014).
61. Chekkoury, A. et al. High-resolution multispectral optoacoustic tomography of the vascularization and constitutive hypoxemia of cancerous tumors. *Neoplasia* **18**, 459–467 (2016).
62. Omar, M., Soliman, D., Gateau, J. & Ntziachristos, V. Ultrawideband reflection-mode optoacoustic mesoscopy. *Opt. Lett.* **39**, 3911–3914 (2014).
63. Omar, M., Gateau, J. & Ntziachristos, V. Raster-scan optoacoustic mesoscopy in the 25-125 MHz range. *Opt. Lett.* **38**, 2472–2474 (2013).
64. Schwarz, M. et al. Optoacoustic dermoscopy of the human skin: tuning excitation energy for optimal detection bandwidth with fast and deep imaging in vivo. *IEEE Trans. Med. Imaging* **36**, 1287–1296 (2017).
65. Berezhnoi, A. et al. Optical features of human skin revealed by optoacoustic mesoscopy in the visible and short-wave infrared regions. *Opt. Lett.* **44**, 4119–4122 (2019).
66. Schwarz, M., Buehler, A., Aguirre, J. & Ntziachristos, V. Three-dimensional multispectral optoacoustic mesoscopy reveals melanin and blood oxygenation in human skin in vivo. *J. Biophotonics* **9**, 55–60 (2016).
67. Berezhnoi, A. et al. Assessing hyperthermia-induced vasodilation in human skin in vivo using optoacoustic mesoscopy. *J. Biophotonics* **11**, e201700359 (2018).
68. Subochev, P. et al. Raster-scan optoacoustic angiography reveals 3D microcirculatory changes during cuffed occlusion. *Laser Phys. Lett.* **15**, 045602 (2018).
69. Cracowski, J. L., Minson, C. T., Salvat-Melis, M. & Halliwill, J. R. Methodological issues in the assessment of skin microvascular endothelial function in humans. *Trends Pharmacol. Sci.* **27**, 503–508 (2006).
70. Jathoul, A. P. et al. Deep in vivo photoacoustic imaging of mammalian tissues using a tyrosinase-based genetic reporter. *Nat. Photonics* **9**, 239–246 (2015).
71. Krumholz, A., Shcherbakova, D. M., Xia, J., Wang, L. V. & Verkhusha, V. V. Multicontrast photoacoustic in vivo imaging using near-infrared fluorescent proteins. *Sci. Rep.* **4**, 3939 (2014).
72. Stiel, A. C. et al. High-contrast imaging of reversibly switchable fluorescent proteins via temporally unmixed multispectral optoacoustic tomography. *Opt. Lett.* **40**, 367–370 (2015).
73. Shi, J. et al. High-resolution, high-contrast mid-infrared imaging of fresh biological samples with ultraviolet-localized photoacoustic microscopy. *Nat. Photonics* **13**, 609–615 (2019).
74. Zhao, Z., Shen, Y., Hu, F. & Min, W. Applications of vibrational tags in biological imaging by Raman microscopy. *Analyst* **142**, 4018–4029 (2017).
75. Walsh, J. P. Managing thyroid disease in general practice. *Med. J. Aust.* **205**, 179–184 (2016).
76. Dima, A. & Ntziachristos, V. In-vivo handheld optoacoustic tomography of the human thyroid. *Photoacoustics* **4**, 65–69 (2016).
77. Roll, W. et al. Multispectral optoacoustic tomography of benign and malignant thyroid disorders–a pilot study. *J. Nucl. Med.* **60**, 1461–1466 (2019).
78. Yang, M. et al. Photoacoustic/ultrasound dual imaging of human thyroid cancers: an initial clinical study. *Biomed. Opt. Express* **8**, 3449–3457 (2017).
79. Zhang, L. & Thurber, G. in *Imaging and Metabolism* (eds. Lewis J. S. & Keshari K. R.) 175–197 (Springer, 2018).
80. Rastogi, R. & Jain, S. K. Imaging in diabetes mellitus. *Arch. Clin. Nephrol.* **2**, 017–025 (2016).
81. Knieling, F. et al. Raster-scanning optoacoustic mesoscopy for gastrointestinal imaging at high resolution. *Gastroenterology* **154**, 807–809 (2018).
82. Gotfried, J., Priest, S. & Schey, R. Diabetes and the small intestine. *Curr. Treat. Options Gastroenterol.* **15**, 490–507 (2017).
83. Hernández-Ochoa, E. O. & Vanegas, C. Diabetic myopathy and mechanisms of disease. *Biochem. Pharmacol.* **4**, 1000e179 (2015).
84. Sörensen, B. M. et al. Prediabetes and type 2 diabetes are associated with generalized microvascular dysfunction. *Circulation* **134**, 1339–1352 (2016).
85. McMillan, D. E. Deterioration of the microcirculation in diabetes. *Diabetes* **24**, 944–957 (1975).
86. Levy, B. I. et al. Impaired tissue perfusion: a pathology common to hypertension, obestiy, and diabetes mellitus. *Circulation* **118**, 968–976 (2008).
87. Fuchs, D., Dupon, P. P., Schaap, L. A. & Draijer, R. The association between diabetes and dermal microvascular dysfunction non-invasively assessed by laser Doppler with local thermal hyperemia: a systematic review with meta-analysis. *Cardiovasc. Diabetol.* **16**, 11 (2017).
88. Fasoula, N.-A. et al. Multicompartmental non-invasive sensing of postprandial lipemia in humans with multispectral optoacoustic tomography. *Mol. Metab.* **47**, 101184 (2021).
89. Diot, G., Dima, A. & Ntziachristos, V. Multispectral opto-acoustic tomography of exercised muscle oxygenation. *Opt. Lett.* **40**, 1496–1499 (2015).
90. Guerrero-Juarez, C. F. & Plikus, M. V. Emerging nonmetabolic functions of skin fat. *Nat. Rev. Endocrinol.* **14**, 163–173 (2018).
91. Miranda, J. J., Taype-Rondan, A., Tapia, J. C., Gastanadui-Gonzalez, M. G. & Roman-Carpio, R. Hair follicle characteristics as early marker of type 2 diabetes. *Med. Hypotheses* **95**, 39–44 (2016).
92. Baltzis, D., Eleftheriadou, I. & Veves, A. Pathogenesis and treatment of impaired wound healing in diabetes mellitus: new insights. *Adv. Ther.* **31**, 817–836 (2014).
93. Rindi, G. et al. A common classification framework for neuroendocrine neoplasms: an International Agency for Research on Cancer (IARC) and World Health Organization (WHO) expert consensus proposal. *Mod. Pathol.* **31**, 1770–1786 (2018).
94. Tummers, W. S. et al. Intraoperative pancreatic cancer detection using tumor-specific multimodality molecular imaging. *Ann. Surg. Oncol.* **25**, 1880–1888 (2018).
95. Lediju Bell, M. A., Ostrowski, A. K., Li, K., Kazanzides, P. & Boctor, E. M. Localization of transcranial targets for photoacoustic-guided endonasal surgeries. *Photoacoustics* **3**, 78–87 (2015).
96. Padhye, V., Valentine, R. & Wormald, P. J. Management of carotid artery injury in endonasal surgery. *Int. Arch. Otorhinolaryngol.* **18**, S173–S178 (2014).
97. Levi, J. et al. Molecular photoacoustic imaging of follicular thyroid carcinoma. *Clin. Cancer Res.* **19**, 1494–1502 (2013).
98. Feng, T. et al. Characterization of bone microstructure using photoacoustic spectrum analysis. *Opt. Express* **23**, 25217–25224 (2015).
99. Clemmensen, C. et al. Coordinated targeting of cold and nicotinic receptors synergistically improves obesity and type 2 diabetes. *Nat. Commun.* **9**, 4304 (2018).
100. Lemes, L. C., Caetano Júnior, P. C., Strixino, J. F., Aguiar, J. & Raniero, L. Analysis of serum cortisol levels by Fourier transform infrared spectroscopy for diagnosis of stress in athletes. *Res. Biomed. Eng.* **32**, 293–300 (2016).
101. Rao, B. et al. Optical resolution photoacoustic microscopy of ovary and fallopian tube. *Sci. Rep.* **9**, 14306 (2019).
102. Buma, T., Conley, N. C. & Choi, S. W. Multispectral photoacoustic microscopy of lipids using a pulsed supercontinuum laser. *Biomed. Opt. Express* **9**, 276–288 (2018).
103. Yakovlev, V. V. et al. Stimulated Raman photoacoustic imaging. *Proc. Natl Acad. Sci. USA* **107**, 20335–20339 (2010).
104. Seeger, M., Karlas, A., Soliman, D., Pelisek, J. & Ntziachristos, V. Multimodal optoacoustic and multiphoton microscopy of human carotid atheroma. *Photoacoustics* **4**, 102–111 (2016).
105. Tserevelakis, G. J., Soliman, D., Omar, M. & Ntziachristos, V. Hybrid multiphoton and optoacoustic microscope. *Opt. Lett.* **39**, 1819–1822 (2014).
106. Kellnberger, S. et al. Optoacoustic microscopy at multiple discrete frequencies. *Light. Sci. Appl.* **7**, 109 (2018).
107. Zhao, H. et al. Motion correction in optical resolution photoacoustic microscopy. *IEEE Trans. Med. Imaging* **38**, 2139–2150 (2019).
108. Schwarz, M., Garzorz-Stark, N., Eyerich, K., Aguirre, J. & Ntziachristos, V. Motion correction in optoacoustic mesoscopy. *Sci. Rep.* **7**, 10386 (2017).
109. Ron, A., Davoudi, N., Deán-Ben, X. L. & Razansky, D. Self-gated respiratory motion rejection for optoacoustic tomography. *Appl. Sci.* **9**, 2737 (2019).
110. Trimboli, P. et al. Ultrasound and ultrasound-related techniques in endocrine diseases. *Minerva Endocrinol.* **43**, 333–340 (2018).
111. Barsanti, C., Lenzarini, F. & Kusmic, C. Diagnostic and prognostic utility of non-invasive imaging in diabetes management. *World J. Diabetes* **6**, 792–806 (2015).
112. De Sanctis, V. et al. Hand X-ray in pediatric endocrinology: skeletal age assessment and beyond. *Indian. J. Endocrinol. Metab.* **18**, S63–S71 (2014).
113. Pisani, P. et al. Screening and early diagnosis of osteoporosis through X-ray and ultrasound based techniques. *World J. Radiol.* **5**, 398–410 (2013).
114. Piciucchi, S., Poletti, V., Sverzellati, N., Gavelli, G. & Carloni, A. Primary and secondary hyperparathyroidism: findings on chest X-rays and high resolution CT. *Eur. J. Radiol. Extra* **70**, e107–e110 (2009).
115. Marmin, C. et al. Computed tomography of the parathyroids: the value of density measurements to distinguish between parathyroid adenomas of the lymph nodes and the thyroid parenchyma. *Diagn. Interv. Imaging* **93**, 597–603 (2012).
116. Wang, F. et al. CT and MRI of adrenal gland pathologies. *Quant. Imaging Med. Surg.* **8**, 853–875 (2018).
117. Stein, A. L., Levenick, M. N. & Kletzky, O. A. Computed tomography versus magnetic resonance imaging for the evaluation of suspected pituitary adenomas. *Obstet. Gynecol.* **73**, 996–999 (1989).
118. Huh, J. et al. Optimal phase of dynamic computed tomography for reliable size measurement of metastatic neuroendocrine tumors of the liver: comparison between pre- and post-contrast phases. *Korean J. Radiol.* **19**, 1066–1076 (2018).
119. Gausden, E. B., Nwachukwu, B. U., Schreiber, J. J., Lorich, D. G. & Lane, J. M. Opportunistic use of CT imaging for osteoporosis screening and bone density assessment: a qualitative systematic review. *J. Bone Jt. Surg. Am.* **99**, 1580–1590 (2017).
120. Nael, K. et al. Dynamic 4D MRI for characterization of parathyroid adenomas: multiparametric analysis. *AJNR* **36**, 2147–2152 (2015).
121. Chang, G. et al. MRI assessment of bone structure and microarchitecture. *JMRI* **46**, 323–337 (2017).
122. Takatsu, Y., Okada, T., Miyati, T. & Koyama, T. Magnetic resonance imaging relaxation times of female reproductive organs. *Acta Radiol.* **56**, 997–1001 (2015).
123. Reznek, R. H. CT/MRI of neuroendocrine tumours. *Cancer Imaging* **6**, S163–S177 (2006).
124. Davidson, C. Q., Phenix, C. P., Tai, T., Khaper, N. & Lees, S. J. Searching for novel PET radiotracers: imaging cardiac perfusion, metabolism and inflammation. *Am. J. Nucl. Med. Mol. Imaging* **8**, 200–227 (2018).
125. Pacak, K., Eisenhofer, G. & Goldstein, D. S. Functional imaging of endocrine tumors: role of positron emission tomography. *Endocr. Rev.* **25**, 568–580 (2004).
126. Lu, F. M. & Yuan, Z. PET/SPECT molecular imaging in clinical neuroscience: recent advances in the investigation of CNS diseases. *Quant. Imaging Med. Surg.* **5**, 433–447 (2015).
127. Ichise, M. & Harris, P. E. Imaging of β-cell mass and function. *J. Nucl. Med.* **51**, 1001–1004 (2010).
128. Bernardo-Filho, M., Santos-Filho, S. D., Fonseca, A. D. S. D., Carter, K. & Missailidis, S. Nuclear medicine procedures for the evaluation of male sexual organs: a brief review. *Braz. Arch. Biol. Technol.* **51**, 13–21 (2008).
129. Hopkins, C. R. & Reading, C. C. Thyroid and parathyroid imaging. *Semin. Ultrasound CT MR* **16**, 279–295 (1995).
130. Brabander, T., Kwekkeboom, D. J., Feelders, R. A., Brouwers, A. H. & Teunissen, J. J. Nuclear medicine imaging of neuroendocrine tumors. *Front. Horm. Res.* **44**, 73–87 (2015).
131. Avram, A. M., Fig, L. M. & Gross, M. D. Adrenal gland scintigraphy. *Semin. Nucl. Med.* **36**, 212–227 (2006).
132. Yao, A., Balchandani, P. & Shrivastava, R. K. Metabolic in vivo visualization of pituitary adenomas: a systematic review of imaging modalities. *World Neurosurg.* **104**, 489–498 (2017).

133. Karlas, A., Reber, J., Liapis, E., Paul-Yuan, K. & Ntziachristos, V. Multispectral optoacoustic tomography of brown adipose tissue. *Handb. Exp. Pharmacol.* **251**, 325–336 (2019).

Acknowledgements
The authors acknowledge the support of funding from European Union's Horizon 2020 research and innovation programme under grant agreement no. 871763 (WINTHER) and from the European Research Council (ERC) under grant agreement no. 694968 (PREMSOT) and from the Deutsche Forschungsgemeinschaft (DFG), Germany (Gottfried Wilhelm Leibniz Prize 2013; NT 3/10-1).

Author contributions
The authors contributed equally to all aspects of the article.

Competing interests
V.N. has stock and stock options in iThera Medical. All other authors declare no competing interests.

Peer reviewer information
Nature Reviews Endocrinology thanks the anonymous reviewers for their contribution to the peer review of this work

Publisher's note
Springer Nature remains neutral with regard to jurisdictional claims in published maps and institutional affiliations.

© Springer Nature Limited 2021, corrected publication 2021